HHS Public Access

Author manuscript

Nat Methods. Author manuscript; available in PMC 2024 July 01.

Published in final edited form as:

Nat Methods. 2024 February ; 21(2): 301–310. doi:10.1038/s41592-023-02126-0.

Smart Lattice Light Sheet Microscopy for imaging rare and complex cellular events

Yu Shi[1,*], **Jimmy S. Tabet**[1,*], **Daniel E. Milkie**[2], **Timothy A. Daugird**[3], **Chelsea Q. Yang**[4], **Alex T. Ritter**[5], **Andrea Giovannucci**[1,‡], **Wesley R. Legant**[1,3,‡]

[1)]Joint Department of Biomedical Engineering, University of North Carolina at Chapel Hill, North Carolina State University, Chapel Hill, NC, USA

[2)]Janelia Research Campus, Howard Hughes Medical Institute, Ashburn, VA 20147, USA

[3)]Department of Pharmacology, University of North Carolina at Chapel Hill, Chapel Hill, NC, USA

[4)]Department of Biochemistry and Biophysics, University of North Carolina at Chapel Hill, Chapel Hill, NC, USA

[5)]Altos Labs, Redwood City, CA, USA

Abstract

Light sheet microscopes enable rapid, high-resolution imaging of biological specimens; however, biological processes span a variety of spatiotemporal scales. Moreover, long-term phenotypes are often instigated by rare or fleeting biological events that are difficult to capture with a single imaging modality. To overcome this limitation, we present smartLLSM, a microscope that incorporates AI-based instrument control to autonomously switch between epifluorescent inverted imaging and lattice light sheet microscopy. We demonstrate the utility of this approach by studying two unique biological processes: cell division and immune synapse formation. In each of these contexts, we demonstrate that smartLLSM provides population-level statistics across thousands of cells and autonomously captures multicolor 3D datasets or 4D time-lapse movies of rare events at rates that dramatically exceed human capabilities. Automating both data acquisition and image analysis allows us to quantify the effects of Taxol dose on spindle structure and kinetochore dynamics in dividing cells and of antigen strength on cytotoxic T lymphocyte engagement and lytic granule polarization at the immune synapse. Overall, this new methodology enables efficient detection of rare events within heterogeneous cell populations and records these processes with high spatiotemporal 4D imaging over statistically significant replicates.

[‡]to whom correspondence should be addressed: legantw@email.unc.edu.

[*]equal contribution

Contributions:

W.R.L. conceived the project. A.G. and J.T. lead the development of the DL-based cell detection and classification pipeline with input and contribution from Y.S. and W.R.L.. D.E.M assisted with integrating the YOLO network together with the microscope control software. T.A.D, C.Y., and A.T.R assisted with sample preparation. Y.S. and W.R.L performed the imaging experiments, analyzed data, and wrote the manuscript with feedback from all authors. W.R.L. supervised and directed the project.

Code Availability:

The source code, annotation GUI, the library of annotated training data, and the trained YOLOv5 network generated in the current study are available at: https://github.com/nel-lab/smartLLSM. Code is provided under The MIT License for open source software, a permissive license approved by the Open Source Initiative. Specific terms can be found here: https://opensource.org/licenses/MIT.

Introduction

Light sheet microscopes offer reduced photobleaching, less phototoxicity, and increased imaging speed compared to widefield or confocal microscopes[1,2]. These advantages permit the visualization of dynamic events ranging from single molecules that diffuse in milliseconds [3–7] to organisms that develop over multiple days[8–11]. However, these advances also present new challenges. First, light sheet microscopes can extract gigabytes per second of information from the specimen which necessitates specialized data storage, visualization, and quantification tools[12]. Second, biological samples can rarely tolerate hardware-limited maximum imaging rates for very long before becoming perturbed by the imaging process[13]. Third, because data is still acquired plane-by-plane, there is an inherent sacrifice between the volumetric sampling rate and the imaging field of view driving a tradeoff between rapid, high-content imaging (images with high spatio-temproal resolution) of a small region vs high-throughput imaging (fast scanning speed) of many samples or replicates. Lastly, the oblique geometry, high-magnification, and limited field of view used by many light sheet microscopes impede the rapid selection of specific cells or regions of interest across a large sample, especially if such cells are rare within a population[6,14–16].

By detecting and responding to specific image features, event-triggered microscopy has emerged as a way to overcome these tradeoffs. Previous demonstrations include: automating confocal imaging experiments on rare cells[17], combining population-level analysis with high-resolution widefield imaging[18] and super-resolution localization microscopy[19], selectively increasing the acquisition rate to capture mitochondrial fission and bacterial cell division events with structured illumination microscopy[20], and switching between diffraction limited and super-resolution stimulated emission depletion modalities when specific spatial signatures are detected within live-cell time-series[21]. Inspired by these recent advances, we sought to determine whether similar approaches could be used to program a self-driving lattice light sheet microscope “smartLLSM” that is capable of searching for specific cells within a population and then automatically capturing 4D light sheet movies of these specimens. We accomplish this by rapidly scanning centimeter-scale specimens via inverted epifluorescent microscopy that captures a large field of view parallel to the coverslip and switching on demand to perform lattice light sheet microscopy (LLSM) at automatically determined fields of view. We control the instrument by feeding images to a fully convolutional machine learning algorithm “You Only Look Once, version 5 (YOLOv5)”[22–24] so that the locations and classes of identified objects from inverted microscopy images can automate the acquisition of desired cells via LLSM. We demonstrate the generality of this approach by studying cell division and immune synapse formation, two distinct biological processes that substantially benefit from the low-phototoxicity imaging afforded by light sheet microscopy[25–28]. SmartLLSM processes hundreds of cells per second, dramatically cuts down user interaction time, and generates statistically significant replicates of rare cellular events. This allows it to dramatically reduce the need for up-front data storage and post-acquisition data mining to draw meaningful biological conclusions.

Results

smartLLSM incorporates a fast and accurate object detector

YOLOv5 must be trained on annotated examples that specify both the bounding box and object class within an image. To train the network to identify mitotic cells, we generated a retinal pigment epithelium cell line stably expressing fluorescent fusions of centromere protein A (CENPA-mNeonGreen) and histone H2B (H2B-mScarlet) to label centromeres/kinetochores and chromosomes respectively. We used chromosome morphology to identify cell state and the inverted epifluorescent microscopy mode of smartLLSM to generate single-channel training data (Fig. 1A). To train the network to identify immune synapses, we generated coverslips containing a 3-color mixture of cytotoxic T lymphocytes (CTLs) and peptide presenting GFP-tagged target cells. CTLs were fluorescently labeled via indirect immunofluorescence to tag receptors on the CTL plasma membrane and lytic granules within the CTL. We used both the CTL plasma membrane and target cell GFP signal to generate two channel training data via inverted epifluorescent microscopy and classified cells using both CTL morphology and CTL/target cell proximity (Fig. 1B). These images, together with annotated bounding box coordinates, and the object classes present in each box were used to train YOLOv5 (Fig. 1C, D). Complete details about training set acquisition and model generation are provided in Methods (Fig. S1 and S2). In total, we annotated ~54,000 RPE cells with approximately 5% comprising different mitotic stages and ~2,600 CTLs and 14,000 target cells with approximately 8% comprising contacting cell pairs or discernable immune synapses. Our trained models achieved an average accuracy of 85% for all mitotic stages and 78% for identifying target cells and immune synapses (Fig. 1E, F). As shown in the confusion matrices, the major sources of misidentification occurred between classes that were visually similar or that did not have clear transitions, even to a human observer (e.g. identifying a prophase cell as an interphase cell, mislabeling metaphase and prometaphase, or misidentifying contacting pairs vs. true immune synapses). Networks trained on subsets representing ~15% of the total training data for each application still functioned within 10% of peak performance suggesting that, depending on the desired accuracy, the instrument can be rapidly trained for new applications using many fewer annotated examples (Fig. S3). Furthermore, precision vs. recall curves, calculated as “one vs. all” for each class, can be used to tune the models to maximize network precision (low false positive rate) or recall (low false negative rate) depending on experimental goals (Fig. 1G, H).

smartLLSM implementation and timing

To demonstrate the utility of smartLLSM, we first highlight its ability to survey large populations of cells and acquire multicolor 3D volumes of selected cells of interest. In this case, we perform a 2D tiled scan of a 16 mm x 6 mm area using inverted epifluorescent microscopy while passing the tiled images to the YOLOv5 network (Fig. 2A). For a typical dataset, we process batches of 100 images in parallel, with each image consisting of 800 x 800 pixels. With a pixel size of 100 nm at the sample, each individual image is an 80 x 80 μm field of view and each batch represents a 10 x 10 tiled array of images from 800 x 800 μm of the sample. When RPE cells are plated at 80% confluence, each image batch contains approximately 300 nuclei and requires 0.84 seconds to process (Fig. S4A). This

yields a network processing rate of ~357 cells per second. For synapse detection, each image batch contains 220 cells on average, and requires 1.85 seconds to process, which yield a processing rate of 120 cells per second. The slower speed for synapse detection is mostly due to increased load during preprocessing to merge images from the two channels into an RGB image while the network's inference speed was similar, (Fig. S4B). Thus in both cases, our processing pipeline dramatically exceeds the rate of manual image inspection.

For fixed specimens, we scan the entire area via 2D inverted epifluorescent microscopy while logging the stage and position of each cell (Fig. 2B). With a camera exposure time of 50 ms, the entire 96 mm^2 imaging region containing approximately 30,000 cells can be scanned with 300 nm lateral resolution in ~15 minutes while processing the resulting 11,400 2D images takes ~10 minutes for cell detection and classification including file input/output overhead. Pipelining image acquisition and network inference in parallel allows for real time processing. Once complete, we then switch to LLSM and return to each cell of interest to perform multicolor 3D imaging (Fig. 2C). For both dividing cells and immune synapses, scanning a 60 μm by 110 μm by 30 μm volume around each cell at 50 ms exposure per plane with three colors via LLSM takes approximately 20 s, although this could be sped up by an order of magnitude or more by shortening the exposure-per-plane, depending on fluorophore brightness and desired imaging quality. Altogether, this application provides automatic and high-throughput 3D imaging of select cells within a population (Movie S1, S2).

smartLLSM to surveil cell populations

To verify that that the trained YOLO network performed as expected, we sought an orthogonal validation that did not rely on user annotation. To this end, we determined the proportion of mitotic cells found by our network when imaging a synchronized cell population compared to a control sample. Under live-cell conditions, we repeatedly imaged a 16 mm x 6 mm area via inverted epifluorescent microscopy once every 30 minutes. The classification network detected a clear mitotic wave in synchronized RPE reporter cells between 10 and 14 hrs after thymidine release whereas this peak was absent in unsynchronized control samples (Fig. S5). In control samples, the ratio of mitotic cells increased slightly over the course of the 18 hr imaging experiment, indicating minimal phototoxicity or perturbation from being maintained in the microscope imaging chamber or from the imaging itself, whereas the network detected very few mitotic events in unreleased cells.

We next sought to demonstrate the advantages of smartLLSM to determine population-level trends introduced either by drug or biological perturbations. We imaged chemically fixed RPE cells expressing CENPA-mNeonGreen and H2B-mScarlet. Across multiple coverslips, we located and classified approximately 180,000 cells of which only ~0.4 percent were in mitosis, which is similar to our live-cell control samples above (Fig. 3A). Of the mitotic cells, the majority were in metaphase (0.195%) while prophase was the rarest sub-class (0.022%). Treatment with a low-concentration, 5 nM dose of Paclitaxel (Taxol), a commonly used chemotherapeutic, significantly reduced the percentage of cells in mitosis ($p = 0.02$) and altered the distribution of cells in each mitotic subclass ($p = 7E-8$ via chi-square test of independence) (Fig. 3A). This implied that, as expected, Taxol-treated cells are

inhibited from progressing through downstream mitotic stages[29,30]. For immune synapses, we compared the effects of target cells expressing different strength activating peptides (High – N, Medium – T, and Low – G)[31,32] and quantified the total number of CTLs, target cells, and the fraction CTLs that either contract a target cell or successfully formed an immune synapse. Across 4 separate coverslips, we detected in total 248,713 target cells and 48,821 CTLs across all conditions (Fig. 3B). Of all "objects" detected on the coverslip, immune synapses represented only 1.4%, demonstrating that these are indeed rare events within a heterogeneous population. These observations allowed us to determine whether differences in target cell antigen strength affect the percentage of CTLs in contact with target cells. We computed the normalized contacting ratio which takes into account the relative densities of both the CTLs and target cells within an experimental condition (Fig. 3B **inset**). Prior studies have suggested that antigen strength can increase the percentage of CTLs forming conjugates[33]. However, other studies have suggested that antigen strength increases synapse signaling, but does not increase the number of synapses formed[34]. Here, we found a weak, but not statistically significant trend, wherein increased antigen strength resulted in a slightly higher propensity for CTLs to be found in contact with target cells. Overall, these data demonstrate that smartLLSM captures changes in the distribution of cellular states within two very different biological systems and under different types of perturbations.

smartLLSM for high-content and high-throughput imaging of specific cells

In addition to population-level statistics, smartLLSM also allows for automated, high-resolution imaging of select cells within a sample. This is in contrast to alternative methods like flow cytometry where it is not possible to revisit individual cells after the initial scan. To demonstrate the utility of this approach, we quantified the sub-cellular effects of Taxol perturbation on specific mitotic stages, by automatically imaging kinetochores, H2B, and microtubules (immunostained for β-tubulin-Alexa647) in prometaphase and metaphase cells using multicolor LLSM (Fig. 3C). We then transformed this collection of 3D LLSM datasets to the same reference frame using the kinetochore distribution and the plane of the metaphase plate as a coordinate origin (Fig. 3D, see Methods for details). When we examined the orientation of the metaphase plate relative to the cover glass, we found a clear reorientation from parallel (in prometaphase) to perpendicular (in metaphase) (Fig. 3E), in agreement with previous observations tracking the spindle pole orientation during these stages[35]. Interestingly, this reorientation was disrupted by exposure to Taxol, leading to a randomly orientated metaphase plate (Fig. 3E). We also found that our control cells displayed a "barrel-like" microtubule and kinetochore distribution that was maximal in prometaphase and was persistent into metaphase. This structure is thought to facilitate accurate chromosome segregation by increasing the probability of correct amphitelic attachments between kinetochores and microtubules[35,36] and was disrupted by low-dose Taxol treatment (Fig. S6A, B). Finally, we found that Taxol treatment decreased the anisotropy of the kinetochore spatial distribution and increased the presence of multipolar (≥3) spindles. These multipolar structures were not present in prophase cells, but peaked to nearly 60% of all cells examined in prometaphase before declining gradually for other mitotic cell stages (Fig. S6C, D).

In a parallel example, we studied the organization of cytotoxic granules that CTLs secrete through the immune synapse to kill target cells. In agreement with prior studies[32,34], we found that strong antigens increased the percentage of synapses with polarized granules delivered to the CTL-target cell interface whereas weak antigens resulted in more heterogeneously distributed granules (Fig. 3F, G, Fig. S7). Interestingly, aside from this polarization we did not observe changes to the amount of granule clustering in CTLs which has been proposed to potentially occur in response to stronger TCR stimulation (Fig. S8)[32]. Overall, our studies demonstrate that smartLLSM can automate high-content imaging and identify subtle perturbations on rare cells or structures within heterogeneous populations.

smartLLSM for automated 4D imaging

Fixed cell imaging provides only a snapshot of a dynamic 3D process. As such, it is difficult to capture transient temporal events and it is impossible to quantify longitudinal changes in single cells. To address this need, we used smartLLSM for event triggered live-cell imaging of cell division utilizing the dual-labeled reporter RPE line described above. In this case, we continuously scanned living cells via 2D inverted epifluorescent microscopy until YOLO detected a cell in prophase. Once a prophase cell was found, a feedback loop drove the stage to the target coordinates (Fig. 4A) and the microscope collected a 50-minute LLSM time-series, which is sufficient to capture a typical mitotic progression (Fig. 4B, Movie S3). Because mitotic cells are especially sensitive to phototoxicity[13], we first utilized smartLLSM to optimize the light dose, exposure time, and imaging rate while ensuring proper cell division (Table S1), settling on a time course of 3 seconds/volume for the first 5 minutes when motion is the most dynamic and then transitioning to a rate of 6 seconds/volume for the following 45 minutes of imaging.

Kinetochores link chromosomes to microtubules to properly partition DNA into the two daughter cells. In mitosis, they travel complex trajectories as the cell transitions through each mitotic stage. By observing kinetochore dynamics, we can gain a better understanding of the biophysical steps required for proper chromosome segregation and of the origin of mitotic errors[25–27,37]. Toward this end, we first examined the instantaneous speed of kinetochores from prophase to prometaphase (Movie S4). Shortly after nuclear envelop breakdown, kinetochores move rapidly inward as they are captured by microtubules[27]. Based upon this, we plotted the kinetochore speed distribution for each of four stages: prophase, contracting, prometaphase, and metaphase, (Fig. S9A, B, Movie S4). We found an increase in kinetochore speed after nuclear envelop breakdown in prophase, but no significant differences between the contracting, prometaphase or metaphase stages. In all cases, kinetochore speed was well above our noise floor of 10 nm/s, estimated by repeatedly imaging chemically fixed cells at different stages (Fig. S10). We next investigated whether kinetochore dynamics might be differentially sensitive to Taxol during specific mitotic stages (Movie S5).

Cells treated with 5 nM Taxol were still able to enter prophase. However, compared to control cells, none of the 5 nM Taxol treated cells progressed through mitosis (33/35 vs. 0/27), typically arresting at the prometaphase to metaphase transition. In contrast, cells treated with 0.5 nM Taxol progressed similarly to control (16/17). Cells treated with 1

nM Taxol lay in between, with roughly one third of the cells completing mitosis and two thirds arresting prior to metaphase (7/23) (Fig. S11). Live kinetochore tracking revealed that metaphase plate reorientation is delayed and diminished under Taxol treated conditions (Fig. 4C, Fig. S12) and that 5 nM Taxol strongly reduced kinetochore speed in prometaphase compared to control cells (Fig. 4D). For 1 nM Taxol treated cells that completed mitosis successfully, there was no significant difference in kinetochore speed at any cell stage, whereas for those that eventually arrested, we observed decreased kinetochore speed during prometaphase with an intermediate magnitude of effect compared to the 5 nM dose. Kinetochore speed during the initial contracting stage of kinetochore motion after nuclear envelop breakdown was less sensitive to Taxol than kinetochore speed during prometaphase, suggesting that other factors besides microtubule dynamics may impact kinetochore motion during this stage.

In addition to quantifying instantaneous kinetochore speed, we can longitudinally track kinetochores. Recent studies have used LLSM and 3D single particle tracking to identify “lazy” or lagging kinetochores which fail to partition into the daughter cells at the same rate during anaphase[37]. Intriguingly, this study revealed that metaphase kinetochore dynamics could be partially predictive of future mislocalizations during anaphase. Here, we track kinetochores in LLSM movies of mitosis and identify outlier kinetochores based on their spatial coordinates (see Methods for details on outlier identification). Once an outlier kinetochore is identified, its trajectory can be analyzed to reveal its behavior before, during, and after it deviated from the population distribution (Fig. 5A, Movie S6). Although we did not observe any significant change in the speed of outlier kinetochores vs. others (Fig. S13), we found that the probability of observing an outlier kinetochore varied at different mitotic stages (Fig. 5B). We did not detect any outliers in prophase, but detected that approximately 1% of kinetochores were outliers in both prometaphase and anaphase. In contrast, only 0.2% of kinetochores are outliers in metaphase (Fig. 5B). Chromosome positions undergo the largest reorganizations during prometaphase and anaphase, so the potential for mitotic errors and for kinetochores to deviate from the expected distribution may be higher in these stages than during metaphase when most chromosomes move relatively little within the metaphase plate. We next examined average duration during which a kinetochore is classified as an outlier. Interestingly, outlier events were longest in metaphase (505.8 s), followed by prometaphase (238.6 s) and shortest in anaphase (78.4 s), indicating that the mechanisms for outlier correction may take longer during metaphase (Fig. 5C). By considering both the number of outlier kinetochores in a given stage, the duration of the outlier events themselves, and the average duration of a mitotic stage, we can compute the instantaneous probability of observing an outlier kinetochore at any instant in time within given cell stage. With this information, we find that at any given time, there is an approximately 0.26%, 0.14%, and 0.20% percent chance to observe an outlier kinetochore in prometaphase, metaphase, and anaphase respectively (Fig. 5D).

Longitudinal tracking also enables us to test additional hypotheses about the search and capture process of kinetochores by microtubules. For example, a recent study suggested that the location of a kinetochore within the interphase nucleus can influence its propensity to missegregate during mitosis[38]. Focusing specifically on kinetochores that could be unambiguously tracked from the start of prophase through to anaphase (Fig. S14), we

tracked 899 trajectories from 33 cells total and plotted the duration, distance traveled, and average speed for each kinetochore as a function of its position within the prophase nucleus. Interestingly, we found no clear correlation between any of these values and the position of the kinetochore in the prophase nucleus (Fig. S15), although it's not immediately clear if this might be due to differences in methodologies between our approach and prior studies.

Discussion

In this work, we combine AI-based computer vision with LLSM to autonomously image rare events in both fixed and live-cell conditions. This system allows for quantification of subtle biological and pharmacological effects to population-level distributions as well as to the sub-cellular organization of stereotypical structures such as the mitotic spindle and the immune synapse. Automated sample search, live imaging, and longitudinal 4D tracking allows quantification of kinetochore trajectories, reveals that certain mitotic stages are more prone to outlier events than others, and explores the effects of drug perturbations on this process. The statistical power of these comparisons arise from thousands of 3D fixed cell datasets and hundreds of 4D live cell movies, that together consist of millions of 2D image planes and over 40 TB of total raw data. By scanning, localizing, and classifying hundreds of cells per second, smartLLSM dramatically exceeds the rate of manual sample search, it reduces the overall data burden, and it enriches the acquired data for specific events of interest.

SmartLLSM builds upon recent work in automated, adaptive, or "self-driving" microscopes[17,20,21,39,40]. In particular, automated sample search and cell classification has been demonstrated previously using object segmentation, feature vector computation, and support vector machines (SVM) on commercially available confocal microscopes[17]. Timing data was not provided in these demonstrations, thus preventing a direct comparison to this work; however, due to the need to first segment cells and then compute feature vectors for each cell independently, our initial trials with SVM-based approaches were over an order of magnitude slower than our implementation with YOLOv5 on the same data. For example, generating the segmentation masks via Cellpose, the first step of our SVM classification test, took roughly 20-fold longer than the entire YOLOv5 pipeline. Although this could be explained in part by the specifics of how these processes were implemented, fully convolutional approaches are well-established to be faster than methods with separate detection and classification steps[23]. Combined with the fact that LLSM can be 1 to 2 orders of magnitude faster than point scanning confocal[6], we estimate that our approach is between 10X - 100X faster than the prior state of the art, while achieving comparable accuracy for automated sample search and 3D imaging (Supplementary Note 1).

While our initial demonstrations focused on mitosis and immune synapse formation, the pipeline can be adapted to any biological phenomena that is stereotypical, morphologically distinct, or that contains a unique combination of image properties. For example, in addition to the examples studied here, the platform can also be used automate more routine laboratory tasks such as quantifying and imaging co-expressing reporter cells within a mixed population while avoiding cells that display overexpression artifacts (Fig. S16). However, a limitation for any supervised learning method, including smartLLSM, is that the network

may behave unpredictably when presented with data that is outside the training dataset. Care must be taken to retrain the network if experimental conditions or the desired cellular events to be captured change. Additionally, the network will still be subject to any user bias present in the annotated training data. There is a risk that by only imaging cells that conform to preconceived ideals, the user may miss cells with unexpected and potentially interesting phenotypes. A lengthier discussion of the tradeoffs and potential caveats of relying on supervised learning for automated imaging is provided in Supplementary Note 2.

Overall, we demonstrate that smartLLSM bridges spatial and temporal scales, enabling mm-scale search and surveillance of cell populations and high-resolution 4D imaging of cellular structures and dynamics. To facilitate the adoption of this approach and aid its adaptation to other types of microscopes, we provide our open-source annotated datasets, the annotation GUI, and the trained networks. We anticipate that this automated approach will increase statistical power for observations of rare cellular events, increase experimental throughput by capturing relevant data at higher speeds than can be achieved via manual sample acquisition, and facilitate the screening of new pharmacological perturbations on a subset of rare cells or cell stages within heterogeneous populations.

Methods:

Neural Network Training

Fig. S1 provides an overview of the training process for the YOLO network. We first collected images via inverted epifluorescent microscopy of the RPE nuclei (Fig. S1A–E) or T cell and target cells (Fig. S1F–I). These images were segmented with the deep-learning based algorithm Cellpose[41] to crop out a bounding box around each cell (Fig. S1B and G). Each cell was then annotated to associate a class to each bounding box (Fig. S1D and H). For mitotic cells, because over 90% of the cells are in interphase, to facilitate manual annotation of the rarer cell stages, we utilized a bootstrap approach to first train a three-state classifier for cells in interphase, mitosis, and a “blurry” class to deal with out of focus regions or non-specific cellular debris (Fig. S1C and Fig. S2). Eventually, the raw images, the bounding boxes, and the associated class of each box are fed into the YOLO network for training. Details of each step are described in the following sections.

i) Segmentation: To train our network, we utilized an initial data set of z-stacks of fixed cells expressing H2B-mScarlet captured through the inverted objective with epi illumination on the lattice light sheet instrument. For a given location, 41 z-planes were acquired at 1 μm spacing and 10 ms exposure to image a full volume above and below the coverslip. The field of view for each z-stack was 800 x 800 pixels in size (80 x 80 μm) and contained approximately 8 cells on average. The stages were then scanned to acquire z-stacks at 23,100 separate positions across the sample. The most in-focus position for each stack was evaluated based on the position with a minimum Shannon Entropy and was used for further processing. This process was repeated for three separate biological replicates. Batches of images were then passed to a pretrained Cellpose network[41]. The algorithm efficiently segmented out potential cells, allowing masks and bounding boxes to be saved for 69,300 individual images. This allowed us to pass individual cells to our cell annotator

and classification networks in subsequent steps. Of note, while Cellpose was able to segment clearly defined cells, it also picked up on blurry cells that lie in different focal planes as well as other non-cellular debris that was picked up while imaging. We utilized general image features (e.g., mask diameter) along with classification categories while annotating (to be learned by the classification network) to account for these blurry cells and erroneous Cellpose masks. To train the YOLO network for detecting immune synapses, we applied a similar imaging scheme except utilizing 2-color rather than single color imaging. We simultaneously imaged target cells and CTLs in different channels, and applied Cellpose to segment out potential cells. All cells segmented in the target cell channels are automatically annotated as target cell, and cells in the CTL channel are annotated manually as described in section iii.

ii) Classification: In order to generate labeled training data from the raw images, we developed a custom interface in Python (Fig. S17). The main GUI consisted of a split view, with the right half displaying the current cell to be labeled and the left half displaying the entire image (with the current cell outlined) to provide local context for the user. This was especially useful when classifying cells in stages such as late anaphase and telophase. In these cases, Cellpose tended to segment the single splitting cell into two separate cells. However, using the global context, it became easy to classify these cells as the second daughter cell could be seen close by the current cell. Moreover, we were able to fine tune our annotation options to account for any artifacts in the Cellpose masks (e.g., debris or cells that were clipped by the edge of an image).

We utilized an iterative approach to bootstrap and expedite annotation of mitotic cells by embedding a neural network within the annotation GUI to “pre-screen” images. Because mitotic cells represent a small fraction of all cells in the images, the class distribution is highly skewed and many images contained only interphase cells. Therefore, we first manually scanned the data to generate a small subset of curated cells (e.g. 10 cells for each class). We used these images to train a three-category neural network classifier that could discriminate between interphase, blurry, and mitotic cells (Fig. S2). Before being passed to the network, we cropped out a 200 x 200 pixel region centered on each cell. Other cells present off-center, but still in the crop, were retained as opposed to masking each individual cell since it seemed to improve classification results. Next, data augmentation was performed using TensorFlow’s “ImageDataGeneration” function. This function preprocessed and augmented the cells via sample-wise standardization and image rotation, flipping, and shearing. The trained network was then implemented in the cell annotator, allowing each image to be “pre-scanned” to determine if the image contained only interphase cells or if cells in any mitotic class were present. This process could be refined by changing the threshold value for classifying cells as mitotic, allowing for a trade-off between the likelihood of images presented to the user containing mitotic cells vs. the likelihood of erroneously discarding useful images to annotate. This allowed for a much more efficient method to acquire training data. This “in-line” neural network was periodically retrained as we acquired more annotated data allowing for more efficient filtering of images and ultimately a more accurate classifier.

iii) Annotation: Fig. S18A shows representative images of the annotated mitotic cells at prophase, prometaphase, metaphase, anaphase, and telophase. We annotated cells as in prophase when clear chromosome condensation is observed, the condensed chromosomes are evenly distributed across the entire cell nuclei, and the overall nucleus shape was ellipsoidal. We annotated prometaphase cells when chromosomes form a ring-like structure and the overall shape of the nucleus deviates from circular but not yet reached a line-like structure. Metaphase cells were defined as nucleus becoming a line-like structure. Anaphase cells were defined as when cells just start to split, with chromosomes in the two daughter cells in close vicinity. Telophase cells were defined as when the chromosomes in the two daughter cells were still condensed, but the two daughter cells were far apart.

For CTLs, we show the representative images of the annotated results in Fig. S18B. We classified CTLs into non-contacting, contacting with target cells, and synapses. We defined CTLs with a clear concave morphology as “synapses” and CTLs that touch but are not conformal along target cell membranes as “contacting”.

iv) YOLO Implementation (smartLLSM Neural Network): Once we obtained the training data, we utilized the state-of-the-art, open-source YOLO architecture[23] to rapidly locate and classify RPE cells within the microscope images into the following categories: interphase, prophase, prometaphase, metaphase, anaphase, telophase, and blurry. We classified cells from the immune synapse substrates as target-cell, CTL-non contacting, CTL-contacting, and CTL-synapse. YOLO is a single-shot detector (it does not have a separate region proposal step), prioritizing detection speed while still maintaining high classification accuracy. We refer the reader to the well-maintained and documented YOLOv5 repository for detailed instructions for training YOLO on custom datasets[24]. In short, we transformed our labeled data to a YOLO-compatible format with uniform square bounding boxes (200 x 200 for mitotic cells and 300 x 300 for T cells, to match our annotation procedure). YOLO is trained on the entire microscope field of view (versus individual cell crops, as per our annotation procedure). We split images into a training (70%, 3981 images for mitotic cells and 2122 images for CTLs) and test set (30%, 1678 images for mitotic cells and 909 for CTLs). In the training set, 33879 total cells were used for mitotic cell detection: 84 anaphase, 5787 blurry, 26284 interphase, 631 metaphase, 293 prometaphase, 258 prophase, and 542 telophase; 11293 total cells were used for synapse detection: 9494 target cells, 872 CTL-non contacting, 499 CTL-contacting, and 428 CTL-synapse. In the test set, 15154 total cells were used for mitotic cell detection: 29 anaphase, 2814 blurry, 11592 interphase, 260 metaphase, 141 prometaphase, 132 prophase, and 186 telophase; 4964 total cells were used for synapse detection: 4176 target cells, 341 CTL-non contacting, 244 CTL-contacting, and 203 CTL-synapses.

We trained the YOLOv5s (“small”) model using default settings for 195 epochs (early stopping, best model used) in 2.8 hours using a Linux workstation equipped with an NVIDIA GeForce RTX 2080 Ti GPU with 12 GB VRAM. Network performance results are shown in Fig. 1E–H. To validate the localization accuracy of YOLO, we compared the center of YOLOs bounding boxes to the center of the original Cellpose masks and found good agreement between YOLO and Cellpose (Fig. S19) which was sufficient for accurately centering the cells for 3D LLSM imaging.

Microscopy optical path

The optical path for smartLLSM is based on a modified version of the instrument described in Chen et al.[6] and Moore RP et al.[42] . Key modifications relevant to this work are the use of a 0.6 numerical aperture (NA) excitation lens (Thorlabs, TL20X-MPL), and 1.0 NA detection lens (Zeiss, Objective W “Plan-Apochromat” x20/1.0, model # 421452-9800), and a matching 1.0 NA objective lens located below the sample to allow for high-resolution epifluorescent inverted imaging. Fig. S20 shows the microscopy optical path. The optical path for lattice light sheet mode is similar to Chen et al, where the light goes through a beam shaping module to illuminate a stripe on a spatial light modulator (SLM). We applied a 0.4/0.3 multi-Bessel lattice on the SLM, and applied the corresponding annular pattern on a mask rotator located in a rear pupil conjugate plane to block the DC component. The light is sent into the excitation objective via the x galvo, and together with the z galvo, it allows scanning of the lattice pattern at the back pupil of the excitation objective (EO). The emitted fluorescence collected by the detection objective (DO) is sent to the camera (Orca Flash 4.0, Hamamatsu) through a tube lens. For the epi-illumination, a flip mirror (FM1) diverts the light to at beam expanding module to illuminate the entire SLM that displays an empty “flat” pattern of uniform grey values. In this mode, the annular mask is rotated to a circular pattern to transmit the DC component of the reflected beam from SLM. The x galvo position is set such that the light path diverts to the inverted objective (IO) through a dichroic rather than EO, and a flipping mirror (FM2) is closed to direct light from IO through a tube lens and onto the same camera that was used for light sheet imaging.

smartLLSM operation

Microscope control is accomplished with a custom developed and freely available LABVIEW software[6]. All samples are mounted to a 25 mm circular coverslip. For inverted imaging, we set the ROI of the camera to 800 by 800 pixels and scanned a tiled array of 10 by 10 positions (in total 800 μm by 800 μm). Inverted imaging was done with an exposure time of 50 ms resulting in approximately 6 s to cover the 800 μm by 800 μm region when including stage settling time. To scan the entire cover glass, we set a list of positions in a 19 by 6 grid covering an area of 16 mm by 6 mm (Fig. 2A). To compensate for any cover glass warping over this large area, we manually tuned the z-focal position in a 3 by 3 grid covering the same area and then fit these positions to a two dimensional second order polynomial to program the z-focal position of each point in the 19 by 6 grid. This 3D position list is then used to perform “Sample Finding” scanning to generate the input data for the deep learning network.

The detection of mitotic cells or immune synapses is done by a Python script that runs in parallel to the LABVIEW instrument control software. Images acquired by LABVIEW are passed to the Python script to be processed by the trained YOLOv5 network. After processing, the Python script outputs a list of coordinates of mitotic cells together with the classification probability from YOLOv5 (Fig. S21). We applied a threshold of 0.2 (for mitotic cells) and 0.8 (for CTLs) on the classification likelihood to filter out false positive detections. The threshold was determined based on manual evaluation of the network performance and the same threshold was applied to both live cell and fixed cell imaging. For cells in anaphase or telophase, the YOLOv5 network tends to independently localize

each of the separated daughter cells. To account for this, we averaged any localizations from these classes that occurred within 10 μm of each other to accurately identify the center of the dividing cell (Fig. S21 d–g). Once a targeted position is generated from the Python script, its coordinates are passed to the Labview software to move the stage to the target position and switch the microscope to LLSM mode. We performed LLSM scanning by moving the sample stage laterally, in the plane of the coverslip, with an "x" step-size of 400 nm (this results in 215 nm translation along the detection optical axis due to an angle of 32.5 degrees between detection focal plan and sample cover glass) over a range of 60 μm. For live-cell imaging, we used a 10 ms exposure time leading to a sampling rate of 2.8 s per volume for the first 100 frames, which typically covers prophase and early prometaphase, and a 20 ms exposure time leading to a sampling rate of 5.8 s per volume for the rest 450 frames, which covers the rest of the mitotic process (in total approximately 50 minutes per cell). This maximizes the sampling rates during prophase to capture the fast-moving kinetochores while minimizing photobleaching and phototoxicity. For fixed cell imaging where rapid acquisition was less critical, we increased the exposure time to 50 ms and utilized sequential exposures for each wavelength to minimize spectral bleedthrough. This resulted in a volumetric sampling time of 22 s per cell. Detailed experimental parameters for all datasets are provided in Table S2.

RPE cell line generation, cell culture, and sample preparation:

All cells used in this study were maintained in hTERT RPE-1 growth media consisting of DMEM/F12 (Thermo Fisher Scientific, 11320033) media supplemented with 10% FBS (Omega Scientific FB-11), 100 U/mL Penicillin-Streptomycin (Thermo Fisher Scientific, 15140122), and 0.01 mg/mL hygromycin B (Thermo Fisher Scientific, 10687010) unless otherwise noted. The cells were cultured in 25 cm^2 or 75 cm^2 dishes without a fibronectin coating. hTERT RPE-1-mScarlet-H2b+mNeon-CENPA cells were generated from parental lines (RRID: CVCL_4388, ATCC) using piggyBac transposon-based methods[43]. The cDNA for mScarlet-H2b and mNeon-CENPA genes was synthesized by GeneScript, then ligated into piggyBac plasmids that conferred resistance to either Blasticidin or Gentymycin[44,45]. 0.3 x 10^6 hTERT RPE-1 cells were electroporated with 1,200 ng of mScarlet-H2b, 1,200 ng of mNeon-CENPA, and 600 ng of piggyBac Transposase (Systems Biosciences, PB210PA-1), using the Neon Transfection system. Immediately following electroporation, cells were plated in 35mm dishes with antibiotic-free hTERT RPE-1 growth media. The media was replaced with fresh antibiotic- free media 6 hours after plating and again the following day. After 48 hours to allow the cells to recover from electroporation, cells were maintained in selection media containing 800 μg/mL of G418 Sulfate (Thermo Fisher Scientific, 10131027) and 6 μg/mL of Blasticidin (Goldbio, B-800-25) for two weeks. The hTERT RPE-1-mScarlet-H2b+mNeon-CENPA cells were then expanded in hTERT RPE-1 growth media and harvested for cryopreservation in a mixture of 40% DMEM/F12, 60% FBS, and 10% DMSO (Millipore-Sigma, D2650-100ML). hTERT RPE-1-mScarlet-H2b+mNeon-CENPA cells were used for experiments for up to 20 passages after thawing.

For transient transfections (Fig. S16), wild-type RPE cells were seeded at a density of 3 x 10^5 cells per well in 12-well plastic dishes 24 hours prior to transfection and incubated at 37°C in a humidified 5% CO2 atmosphere. On the day of transfection, three distinct DNA

plasmid solutions were prepared in Opti-MEM (Thermo Fisher Scientific, 31985070): one with 100 ng of GFP-Sec61b (Addgene Plasmid #121159), another with 100 ng of Halo Tag-Tomm20 (Addgene Plasmid #123284), and a third mixture containing 100 ng each of GFP-Sec61b and HaloTag-Tomm20. Transfections were performed using the Lipofectamine 3000 system (Thermo Fisher Scientific, L3000001) in accordance with the manufacturer's protocol. Sixteen hours post-transfection, the cell media was replaced with pre-warmed growth medium and the cells were allowed to recover for an additional eight hours. Cells were then harvested, combined, and plated on fibronectin-coated #2 coverslips as previously described.

For imaging, 25 mm #2 coverslips (Warner Instruments, 640722) were sonicated in 1M KOH (Millipore-Sigma 484016-1KG) for 30 minutes, washed with diH2O then sonicated in diH2O for 30 minutes. Immediately after sonication in diH2O, cover slips were dried with compressed nitrogen then stored a plastic dish lined with lens paper for a maximum of three weeks. One day prior to imaging experiments, cleaned coverslips were incubated with 10 μg/mL of fibronectin (Stemcell Technologies, 07159)) at 37°C for 30 minutes. Immediately thereafter, hTERT RPE-1-mScarlet-H2b+mNeon-CENPA cells were plated on fibronectin coated coverslips at a density of 3.4 x 10^4 cells/cm^2.

CTL generation and culture:

To generate CTLs from OT-I mice (Jackson Labs), splenocytes were isolated and stimulated with 10nM OVA257-264 peptide (AnaSpec, Fremont, CA, USA) in T cell media (Iscove's Modified Dulbecco's medium (IMDM, Gibco) plus 10% fetal bovine serum (FBS, Cytivia Life Sciences), 2mM L-glutamine (Gibco), 1mM sodium pyruvate (Gibco), 1X MEM non-essential amino acids (Gibco), 50U/mL penicillin/streptomycin (Gibco), and 50μM β-mercaptoethanol (ThermoFisher)). After 48 hours of stimulation, cells were washed and resuspended in T cell media plus 10 IU/mL recombinant human IL-2 (rhIL-2, R&D systems) and seeded in fresh media at 0.5x10^6 cells/mL every 48 hours. Animals were maintained in accordance with the Guide for the Care and Use of Laboratory Animals. Altos Labs is an AAALAC-accredited facility and all animal activities in the research studies were conducted under protocols approved by the Altos Labs Institutional Animal Care and Use Committee (IACUC).

Target Cell Line:

The MC57G murine cancer cell line was maintained in DMEM (Gibco) with 10% FBS and 50U/mL penicillin/streptomycin. The piggybac transposase system (Hera Biolabs) was used to generate the MC57G-EGFP cell line. The sequence coding for EGFP was synthesized de novo and cloned into a piggybac expression vector preceded by an EF1α promoter. Synthesis and cloning performed by Genscript USA, Inc. The MC57G cell line was transfected with piggybac-EF1α_EGFP using Lipofectamine 3000 (Invitrogen) according to the manufacturer's protocol. One week following transfection, EGFP+ cells were sorted by FACS. The MC57G-EGFP cell line was a bulk sorted, polyclonal cell line.

T cell/Cancer cell Sample Preparation:

To investigate the dependence of TCR:peptide-MHC affinity on lytic granule polarization, in-vitro activated CTLs from OT-I mice were combined with adherent MC57G-EGFP cells that present MHC-bound peptides with varying affinity for the OT-I TCR. MC57G-EGFP cells suspended in cRPMI were incubated with the peptides SIINFEKL(high affinity), SIITFEKL(medium affinity), or SIIGFEKL(low affinity) peptides (Anaspec) at 1μM concentration complete DMEM at 37°C for 30 minutes, washed three times, and resuspended in phenol red-free DMEM with 2% FBS (imaging media). $5x10^5$ cells were added to wells of a 6-well plate. Each well contained a single 25mm round #1.5 coverglass (Thomas Scientific) coated with human Fibronectin (Corning). The MC57G-EGFP cells were allowed to settle and adhere for 2 hours in an incubator at 37°C/5% CO2. After this time, $5x10^5$ OT-I CTLs in 0.5mL imaging media were added to each well and the plate was returned to the incubator. The CTLs were allowed 15 minutes to find and engage their targets before fixation.

Taxol Treatment:

Two days prior to imaging experiments, hTERT-RPE-1-mScarlet-H2b+mNeon-CENPA cells were plated on fibronectin coated coverslips at a density of 1.7×10^4 cells/ cm^2. One day prior to imaging experiments, media was replaced with hTERT RPE-1 growth media supplemented with 5 nM Taxol (Millipore-Sigma, PHL89806-10MG). Cells were maintained in Taxol supplemented media for 20 hours. For live-cell experiments, cells were imaged in FluoroBrite (Thermo Fisher Scientific), A1896701) supplemented with 10% FBS, 100 U/mL Penicillin-Streptomycin and 5 nM Taxol. For fixed cell experiments, cells were washed once with 37°C PBS and immediately fixed in a 4% paraformaldehyde-PBS (Thermo Fisher Scientific, 50-980-487) solution for 12 minutes at room temperature. Cells were washed once with PBS for 10 seconds followed by 3 washes with PBS for 5 minutes. Following the final wash step, cells were stored for a maximum of 72 hours at 4° C prior to imaging.

Immunofluorescence:

hTERT RPE-1-mScarlet-H2b+mNeon-CENPA cells were plated on fibronectin-coated dishes at the specified cell densities and times above prior to immunostaining. The cells were washed once with 37°C PBS and immediately fixed in a 4% paraformaldehyde-PBS solution for 12 minutes at room temperature. The cells were then washed with PBS and permeabilized with a 0.5% Triton-PBS (VWR, 0694-1L) solution for 20 minutes. The cells were washed with PBS and blocked in a normal goat serum-PBS (NGS-PBS) (Thermo Fisher Scientific, ICN642921) solution for 1 hour. The cells were then incubated in a 1:250 Anti-β-Tubulin mouse monoclonal antibody (Millipore-Sigma, T5293-.2ML)-NGS-PBS solution for 2 hours. The cells were washed with PBS and incubated with a 1:500 solution of Alexa Fluor 647 (Thermo Fisher Scientific, A-21245) conjugated goat anti-mouse secondary antibody NGS-PBS solution for 2 hours. Cells were washed with PBS and stored for a maximum of 48 hours at 4° C prior to imaging. To minimize the loss of less-adherent mitotic cells, all incubation steps were performed without rocking and all aspiration steps were performed using a pipette instead of a vacuum. The protocol for all PBS wash steps,

except for the initial washing prior to fixation, consisted of 1 wash with PBS for 10 seconds followed by 3 washes with PBS for 5 minutes. All steps were performed at room temperature unless otherwise noted.

CTL and target cell substrates were fixed with PBS containing 4% PFA (Thomas Scientific) for 10 minutes. Cells were permeabilized for 10 minutes with Cytofix/Cytoperm solution (BD Biosciences) and subsequently stained with antibodies against mouse Granzyme B (APC, Biolegend) and mouse CD8E (PE, Biolegend). Antibody incubation and subsequent washes were performed in Perm/Wash Buffer (BD Biosciences).

Cell synchronization

Four days prior to imaging, hTERT-RPE-1-mScarlet-H2b + mNeon-CENPA cells were plated on fibronectin coated coverslips at a density of 6000 cells/ cm^2 for thymidine (Sigma, T9250) blocked samples and 3000 cells/cm^2 for control samples. On day 2 after plating, media for the thymidine blocked samples was replaced with 8 nM thymidine supplemented media. Control cells received fresh media. Cells were allowed to incubate for 18 hours. After 18 hours, all samples were washed 3 times with warm media and received fresh media. Cells were allowed to incubate for 8 hours. Media for the thymidine blocked samples was then replaced with 8 nM thymidine supplemented media and control cells received fresh media. Cells were again allowed to incubate for 18 hours. After 18 hours, all samples were washed 3 times with warm media and received fresh growth media. Cells were then allowed to incubate for 5 hours before being moved to the microscope for imaging.

Imaging processing, kinetochore tracking and trajectory quantification

Because of the angle between the detection focal plane and the sample plane, raw lattice light sheet images are first deskewed[6]. The deskewed images are then deconvolved with the corresponding experimentally measured point spread function using Richard-Lucy method for 10 iterations[46].

i) Kinetochore localization and tracking: For kinetochore localization, we applied a difference of Gaussian filter to the 3D deconvolved images of the kinetochore channel and then fit the local maxima of each spot with a 3D Gaussian function using a maximum likelihood estimator (MLE). To track kinetochores across time points, we utilized a modified Matlab code based on uTrack[47] with a maximum search radius of 10 pixels (~ 1 μm). To remove spurious localizations, we discarded any tracks with a length less than 10 frames. To identify the cell stage from the live-cell time lapse movies of kinetochore trajectories, we manually determined the first frame corresponding to the onset of mitotic stage based on kinetochore motion and organization. We defined the “contracting stage” as the starting point where kinetochores move rapidly inward after prophase, prometaphase as the endpoint of this contracting process, metaphase as the time point where all kinetochores aligned to the metaphase plate and anaphase as the time where kinetochores start to move outward toward the two daughter cells (Movie S3).

ii) Quantification of kinetochore spatial distribution and metaphase plate orientation: To compensate for varying cellular orientation and to quantify changes in the

kinetochore arrangement under different conditions, we first applied principal component analysis of the localizations of kinetochores in each image using the PCA function in Matlab (The Mathworks). This function extracts the eigenvalues, the eigenvectors, and the projected coordinates of the localizations to the eigenvectors of the data. The orientation of the metaphase plate (θ, Fig. 3D, E) is defined as the angle between the normal vector of the sample plane (in our case the z direction) and the eigenvector associated with the smallest eigenvalue. These values provide a normalized metaphase plate reference frame (defined as the projected coordinates along the first and second eigenvectors) that can be used to register other channels within the same dataset. The normalized variation of kinetochore coordinates along the first and second eigenvectors respectively can be used to define an affine transform, $x'_i = \frac{\vec{r} \cdot \vec{e}_i}{E_i}$, where $\vec{r}$ is the kinetochore location in the camera coordinate, and $\vec{e}_i$ is the ith eigenvector and is the ith eigenvalue. This transform operates on either the 3D point cloud of kinetochore locations or on the pixel coordinates within the images themselves. This affine transform can then be used to rotate and stretch the images of chromosomes, microtubules, and kinetochores to register them into the same coordinate frame and account to variations in cellular orientation and size. We generated heatmap images of the distributions for kinetochores, chromosomes, and microtubules based on the histogram of positions (kinetochores) or immunofluorescence intensity (chromosomes and microtubules) aggregated across all cells in each condition (Fig. S6A).

We quantified the anisotropy of the kinetochore distribution (Fig. S6C) as $A = \frac{l_1 + l_2}{2l_3}$, where l_1, l_2, and l_3 are the largest to smallest ordered eigenvalues respectively. To quantify the orientation of the metaphase plate in live-cell movies, we plotted the metaphase plate orientation (defined above) and as a function of time after the start of prometaphase (Fig. 4C). We then fit the metaphase plate orientation vs. time curve from each cell to a sigmoid function, which follows the form of $\theta = \theta_0 + H * \frac{1}{1 + e^{-(\frac{x - x_0}{D})}}$ (Fig S12). From these fits, we extracted the total reorientation angle H and the time at which the reorientation finishes (defined as $x_0 + D$).

iii) Calculation of kinetochore speed: To compensate for the uneven sampling rate during prophase and the rest of the mitotic process (2.8 s per volume for the first 100 frames and 5.8 s per volume for the last 450 frames), we first interpolated the kinetochore tracks over the first 100 frames using a sampling rate of 5.8 s per volume. To compensate for global cell motion or microscope drift, we subtracted the average translational motion of all kinetochores between frames. We then calculated kinetochore speed as the distance a kinetochore traveled between two neighboring interpolated frames.

To segment the speed distribution at different mitotic stages, we manually annotated the onset of contracting, prometaphase, metaphase and anaphase in each mitotic cell time-lapse as described above. For the non-splitting cells treated with 1 nM or 5 nM Taxol, there is no anaphase onset time point. To generate probability distributions of the kinetochore speed, we aggregated the computed speed at each time point in a given mitotic stage of all kinetochores across all cells. To generate the box plot of medians of the velocity distribution,

we calculated the median velocity of all kinetochores within each cell across all time points for a given mitotic stage.

iv) Outlier kinetochore detection: Because there can occasionally be extra cells present within a live-cell movie in addition to the mitotic cell of interest, we first identified the kinetochores corresponding only to the mitotic cell of interest by applying the DBSCAN function in Matlab with a search radius of 50 pixels (5.4 μm) and a minimum cluster size of 50 points. Localizations within the largest cluster correspond to the dividing cell of interest and are utilized for further analysis. To account for spurious localizations that may results from camera noise or other sources, we additionally filtered localizations to only include tracks with a minimum length of 10 frames. We then project the remaining kinetochore localizations along the eigenvectors based on PCA analysis described above, and applied "rmoutliers" function in Matlab to detect abnormal kinetochores. We used "gesd" method (generalized extreme studentized deviate test) with a detection threshold of 0.05. For time points after the anaphase onset, we detect the two daughter cells usingthe DBSCAN function in matlab with a search radius of 40 pixels (4.3 μm) and a minimum cluster size of 40 points and then detect outliers for each cluster using the same "rmoutliers" function as described above. The probability for observing an outlier kinetochore at a given stage is calculated as $\frac{\sum D_i}{N_{KT} * D_{stage}}$, where D_i indicates the duration of an outlier over which kinetochore i was considered an outlier, N_{KT} is the total number of kinetochores in a cell and D_{stage} is the duration of a specific mitotic stage.

v) Analysis of longitudinal kinetochore tracks: To analyze the relationship between kinetochore location during prophase and kinetochore dynamics and location in the metaphase plate, we only included kinetochores with trajectories that span all time points from prophase to the onset of metaphase. We calculated the Mahalanobis distance of each kinetochore to the group centroid and normalized it to a value between 0 and 1 (0 for the kinetochore at the center and 1 for the kinetochore at the edge). To calculate the time point where the kinetochore reaches the metaphase plate, we generate the convex hull that covers the kinetochore distribution during metaphase, and detected the first time point when the kinetochore is included in the convex hull. We then calculated the traveled contour length of the kinetochore trajectory and the median instantaneous speed throughout each kinetochore track.

vi) CTL granule polarization: To quantify the granule polarization in CTLs, we first applied the "imbinarize" function in matlab to generate the masks for CTL and target cells. We then followed the same method as kinetochore localization to localize CTL granules within the mask of CTLs. Next, we calculated the distance of each granule to the CTL centroid, projected it along the vector connecting the centroid of the CTL and the centroid of the target cells that are defined by the mask, and then normalized by the radius of the CTL (See Fig. 3F). The mathematical form of this normalized distance is $R_{norm} = \frac{\left|\left(\vec{r}_{granule} - \vec{r}_{CTL}\right) \cdot \left(\vec{r}_{target} - \vec{r}_{CTL}\right)\right|}{R_{CTL} * \left|\left(\vec{r}_{target} - \vec{r}_{CTL}\right)\right|}$, where $\vec{r}_{granule}$ is the localization of CTL granules, $\vec{r}_{CTL}$ is the localization of CTL centroid, $\vec{r}_{target}$ is the localization of target centroid, and R_{CTL} the

radius of CTL cells. |…| indicates norm of the vector. Rnorm typically falls between −1 to +1with positive Rnorm meaning the granule is close to the target-CTL interface (front of the CTL), and negative R_{norm} meaning the granules is at the back of CTL. Next, we assemble R_{norm} for all granules in the CTL, compute its histogram, and categorize the synapse type based on the location of the highest peak in the histogram (Fig 3F and Fig. S7). If the location of the peak is larger than 0.3, we called it “front”, as the granules concentrated at the front of CTL; if the location of the peak is less than −0.3, we called it “back”; if the location of the peak falls between −0.3 to 0.3, we called it “middle”.

Statistics and reproducibility

No statistical method was used to predetermine the sample size. Data sets for fixed cells were repeated for three independent biological replicates each with two cover glass samples for each condition. Data for mitotic wave detection was repeated for two biological replicates with one coverslip for each replicate and condition. Datasets for live cell movies comparing control and Taxol conditions were repeated for three independent biological replicates for each condition.

For fixed samples, we used a T-test to compare the proportion of cells in each mitotic stage between control and Taxol treated conditions and a chi-square test of independence to determine whether there is a change in the overall distribution of mitotic stages between control and Taxol conditions (Fig. 3A). We used a Kolmogorov-Smirnov test to determine if there are differences in the distribution of the metaphase plate orientation and kinetochore anisotropy between control and Taxol conditions (Fig. 3E, Fig S6C. We used a T-test to compare if there is a difference between the ratio of CTL contacting with target cells between different target cell antigen strength (Fig 3B). We used a Kolmogorov-Smirnov test to test if there is a difference in CTL granule polarization between different target cell antigen strength (Fig. 3F).

For live-cell movies, we used a T-test to compare if there is a significant difference in the median kinetochore speed between control and various Taxol-treated conditions and to compare if there is a significant difference in the parameters extracted from sigmoid fits of the metaphase orientation curves (Fig. 4C, Fig. S12). We used a Kolmogorov-Smirnov test to determine if there is a significant difference between the probability, duration, and normalized probability of abnormal kinetochores in different mitotic stages (Fig. 5B–D). We used linear regression to test if there is a linear relationship between a kinetochore’s position in prophase and the traveled distance, the duration, and the speed of the kinetochore between prophase and metaphase (Fig. S15).

Supplementary Material

Refer to Web version on PubMed Central for supplementary material.

Acknowledgements:

We thank Katelyn Heath, Michaela Clynes, and Victoria Augoustides for assistance with annotating images. We thank Dr. Gokul Upadhyayula for assistance with the single particle tracking code and Dr. Tarun Kapoor, Dr. Michael Emanuele, and Dr. Adam Palmer for helpful discussions and feedback on the manuscript. This work was

funded in part by grants from the National Institutes of Health (1DP2GM136653) awarded to W.R.L.. W.R.L. acknowledges additional support from the Searle Scholars program, the Beckman Young Investigator Program, and the Packard Fellowship for Science and Engineering.

Data Availability:

Due to the inordinate size of the image data (~40TB), it is not currently feasible to deposit this into a central repository; however, all datasets underlying the results in this manuscript are available from the corresponding author upon request. To the extent possible, the authors will try to meet all requests for data sharing within 2 weeks from the original request.

References:

1. Power RM & Huisken J A guide to light-sheet fluorescence microscopy for multiscale imaging. Nat. Methods 14, 360–373 (2017). [PubMed: 28362435]
2. Hobson CM et al. Practical considerations for quantitative light sheet fluorescence microscopy. Nat. Methods 19, 1538–1549 (2022). [PubMed: 36266466]
3. Liu Z. et al. 3D imaging of Sox2 enhancer clusters in embryonic stem cells. eLife 3, e04236 (2014). [PubMed: 25537195]
4. Gustavsson A-K, Petrov PN, Lee MY, Shechtman Y & Moerner WE 3D single-molecule super-resolution microscopy with a tilted light sheet. Nat. Commun 9, 123 (2018). [PubMed: 29317629]
5. Legant WR et al. High-density three-dimensional localization microscopy across large volumes. Nat. Methods 13, 359–365 (2016). [PubMed: 26950745]
6. Chen B-C et al. Lattice light-sheet microscopy: Imaging molecules to embryos at high spatiotemporal resolution. Science 346, (2014).
7. Chen J. et al. Single-Molecule Dynamics of Enhanceosome Assembly in Embryonic Stem Cells. Cell 156, 1274–1285 (2014). [PubMed: 24630727]
8. Keller PJ, Schmidt AD, Wittbrodt J & Stelzer EHK Reconstruction of Zebrafish Early Embryonic Development by Scanned Light Sheet Microscopy. Science 322, 1065–1069 (2008). [PubMed: 18845710]
9. McDole K. et al. In Toto Imaging and Reconstruction of Post-Implantation Mouse Development at the Single-Cell Level. Cell 175, 859–876.e33 (2018). [PubMed: 30318151]
10. Huisken J, Swoger J, Del Bene F, Wittbrodt J & Stelzer EHK Optical Sectioning Deep Inside Live Embryos by Selective Plane Illumination Microscopy. Science 305, 1007–1009 (2004). [PubMed: 15310904]
11. Liu T-L et al. Observing the cell in its native state: Imaging subcellular dynamics in multicellular organisms. Science 360, eaaq1392 (2018). [PubMed: 29674564]
12. Reynaud EG, Peychl J, Huisken J & Tomancak P Guide to light-sheet microscopy for adventurous biologists. Nat. Methods 12, 30–34 (2015). [PubMed: 25549268]
13. Laissue PP, Alghamdi RA, Tomancak P, Reynaud EG & Shroff H Assessing phototoxicity in live fluorescence imaging. Nat. Methods 14, 657–661 (2017). [PubMed: 28661494]
14. Sapoznik E. et al. A versatile oblique plane microscope for large-scale and high-resolution imaging of subcellular dynamics. eLife 9, e57681 (2020). [PubMed: 33179596]
15. Kumar A. et al. Dual-view plane illumination microscopy for rapid and spatially isotropic imaging. Nat. Protoc 9, 2555–2573 (2014). [PubMed: 25299154]
16. Dean KM, Roudot P, Welf ES, Danuser G & Fiolka R Deconvolution-free Subcellular Imaging with Axially Swept Light Sheet Microscopy. Biophys. J 108, 2807–2815 (2015). [PubMed: 26083920]
17. Conrad C. et al. Micropilot: automation of fluorescence microscopy-based imaging for systems biology. Nat. Methods 8, 246–249 (2011). [PubMed: 21258339]
18. André O, Ahnlide JK, Norlin N, Swaminathan V & Nordenfelt P Data-driven microscopy allows for automated context-specific acquisition of high-fidelity image data. Cell Rep. Methods 0, (2023).

19. Barentine AES et al. An integrated platform for high-throughput nanoscopy. Nat. Biotechnol 1–8 (2023) doi:10.1038/s41587-023-01702-l. [PubMed: 36653493]
20. Mahecic D. et al. Event-driven acquisition for content-enriched microscopy. Nat. Methods 1–6 (2022) doi:10.1038/s41592-022-01589-x. [PubMed: 35017739]
21. Alvelid J, Damenti M, Sgattoni C & Testa I Event-triggered STED imaging. Nat. Methods 1–8 (2022) doi:10.1038/s41592-022-01588-y. [PubMed: 35017739]
22. Bochkovskiy A, Wang C-Y & Liao H-YM YOLOv4: Optimal Speed and Accuracy of Object Detection. Preprint at 10.48550/arXiv.2004.10934 (2020).
23. Redmon J, Divvala S, Girshick R & Farhadi A You Only Look Once: Unified, Real-Time Object Detection, in 2016 IEEE Conference on Computer Vision and Pattern Recognition (CVPR) 779–788 (2016). doi:10.1109/CVPR.2016.91.
24. Jocher G. YOLOv5 by Ultralytics. (2020) doi:10.5281/zenodo.3908559.
25. Yamashita N. et al. Three-dimensional tracking of plus-tips by lattice light-sheet microscopy permits the quantification of microtubule growth trajectories within the mitotic apparatus. J. Biomed. Opt 20, 101206 (2015). [PubMed: 26527322]
26. Pamula MC et al. High-resolution imaging reveals how the spindle midzone impacts chromosome movement. J. Cell Biol 218, 2529–2544 (2019). [PubMed: 31248912]
27. David AF et al. Augmin accumulation on long-lived microtubules drives amplification and kinetochore-directed growth. J. Cell Biol 218, 2150–2168 (2019). [PubMed: 31113824]
28. Ritter AT et al. Actin Depletion Initiates Events Leading to Granule Secretion at the Immunological Synapse. Immunity 42, 864–876 (2015). [PubMed: 25992860]
29. Ikui AE, Yang C-PH, Matsumoto T & Band S Low Concentrations of Taxol Cause Mitotic Delay Followed by Premature Dissociation of p55CDC from Ma. Cell Cycle 4, 5.
30. Brito DA & Rieder CL The Ability to Survive Mitosis in the Presence of Microtubule Poisons Differs Significantly Between Human Nontransformed (RPE-1) and Cancer (U2OS, HeLa) Cells. Cell Motil. Cytoskeleton 66, 437–447 (2009). [PubMed: 18792104]
31. Denton AE et al. Affinity Thresholds for Naive CD8+ CTL Activation by Peptides and Engineered Influenza A Viruses. J. Immunol 187, 5733–5744 (2011). [PubMed: 22039305]
32. Frazer GL, Gawden-Bone CM, Dieckmann NMG, Asano Y & Griffiths GM Signal strength controls the rate of polarization within CTLs during killing. J. Cell Biol 220, e202104093 (2021). [PubMed: 34292303]
33. Yachi PP, Ampudia J, Zal T & Gascoigne NRJ Altered Peptide Ligands Induce Delayed CD8-T Cell Receptor Interaction—a Role for CD8 in Distinguishing Antigen Quality. Immunity 25, 203–211 (2006). [PubMed: 16872849]
34. Jenkins MR, Tsun A, Stinchcombe JC & Griffiths GM The Strength of T Cell Receptor Signal Controls the Polarization of Cytotoxic Machinery to the Immunological Synapse. Immunity 31, 621–631 (2009). [PubMed: 19833087]
35. Magidson V. et al. The spatial arrangement of chromosomes during prometaphase facilitates spindle assembly. Cell 146, 555–567 (2011). [PubMed: 21854981]
36. Chaly N & Brown DL The prometaphase configuration and chromosome order in early mitosis. J. Cell Sci 91, 325–335 (1988). [PubMed: 3076886]
37. Sen O, Harrison JU, Burroughs NJ & McAinsh AD Kinetochore life histories reveal an Aurora-B-dependent error correction mechanism in anaphase. Dev. Cell (2021) doi:10.1016/j.devcel.2021.10.007.
38. Klaasen SJ et al. Nuclear chromosome locations dictate segregation error frequencies. Nature 1–6 (2022) doi:10.1038/s41586-022-04938-0.
39. Royer LA et al. Adaptive light-sheet microscopy for long-term, high-resolution imaging in living organisms. Nat. Biotechnol 34, 1267–1278 (2016). [PubMed: 27798562]
40. Eisenstein M. Smart solutions for automated imaging. Nat. Methods 17, 1075–1079 (2020). [PubMed: 33077968]
41. Stringer C, Wang T, Michaelos M & Pachitariu M Cellpose: a generalist algorithm for cellular segmentation. Nat. Methods 18, 100–106 (2021). [PubMed: 33318659]

42. Moore RP et al. A multi-functional microfluidic device compatible with widefield and light sheet microscopy. Lab. Chip 22, 136–147 (2021). [PubMed: 34859808]

43. Ding S. et al. Efficient Transposition of the piggyBac (PB) Transposon in Mammalian Cells and Mice. Cell 122, 473–483 (2005). [PubMed: 16096065]

44. Yeo NC et al. An enhanced CRISPR repressor for targeted mammalian gene regulation. Nat. Methods 15, 611–616 (2018). [PubMed: 30013045]

45. Kirk JM et al. Functional classification of long non-coding RNAs by k-mer content. Nat. Genet 50, 1474–1482 (2018). [PubMed: 30224646]

46. Shao L, Milkie D & Lambert T cudadecon. (2023) doi:10.5281/zenodo.7659013.

47. Jaqaman K. et al. Robust single-particle tracking in live-cell time-lapse sequences. Nat. Methods 5, 695–702 (2008). [PubMed: 18641657]

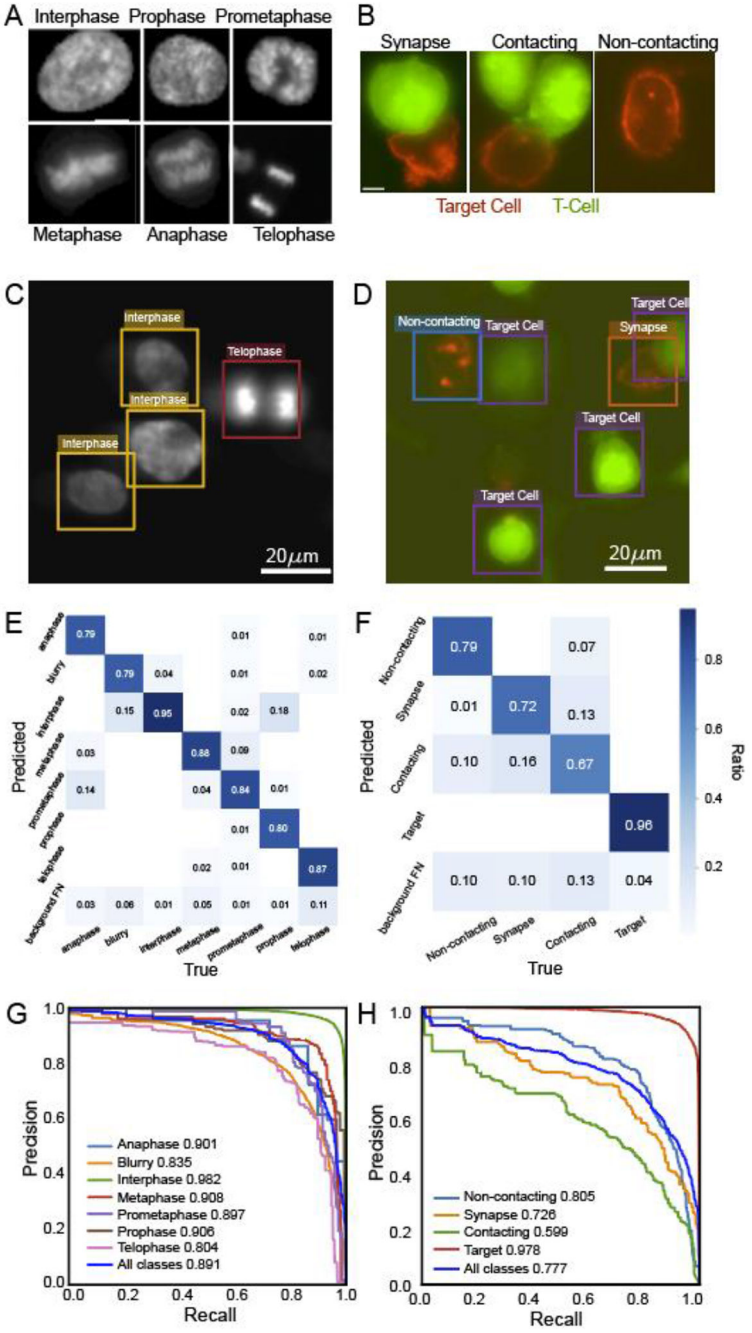

Figure 1: smartLLSM training and performance.

(A) Sample classes for cells in different mitotic stages. **(B)** Sample classes for different CTLs. **(C, D)** Sample output from trained YOLO network to detect mitotic cells and CTLs forming synapses. **(E, F)** Confusion matrix for test images across all detected classes. "Background FN" stands for background false negative, meaning ground-truth labeled cells are misidentified as background. **(G), (H)** Precision vs. recall curves for each detected class. The numbers in the legend indicate the area under each curve.

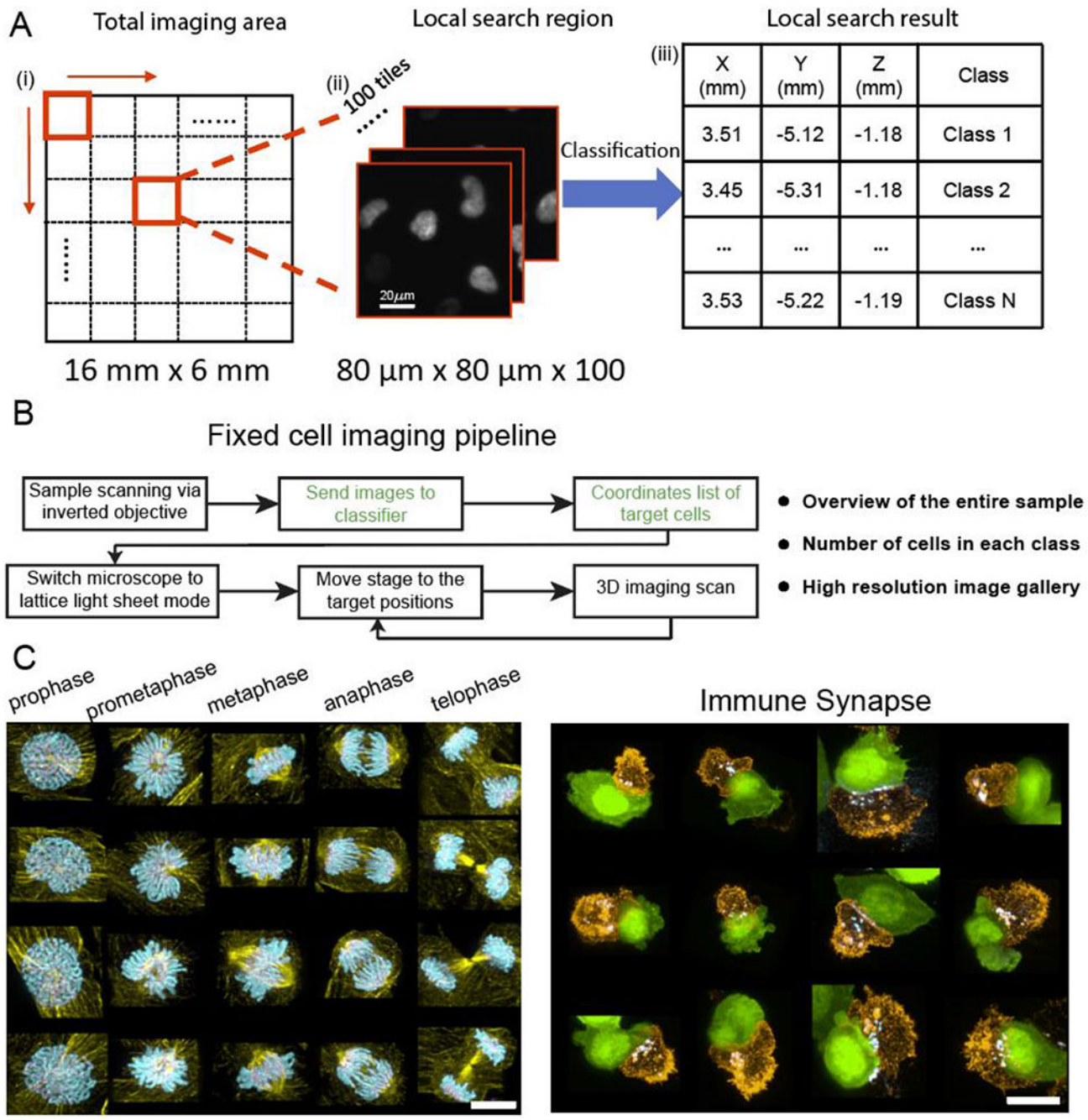

Figure 2: smartLLSM workflow.

(A) Flowchart for smartLLSM imaging. (i) A total imaging area of 16 mm by 6 mm is segmented into a grids of 800 μm by 800 μm squares. (ii) At each location, 100 images of 80 μm by 80 μm fields of view are imaged via inverted epifluorescence microscopy. (iii) These images are sent to the YOLOv5 network to extract the location and associated class for each cell. **(B)** Flow chart for imaging fixed samples. After scanning is complete, the microscope switches to LLSM imaging to acquire a gallery of 3D image scans for each cell stage of interest. **(C)** Mitotic cell images show chromosomes (cyan), kinetochores (magenta), and

microtubules (yellow). CTL Images show MC57 target cells (green), CTLs (orange), and granules (cyan). Scale bars - 10 μm.

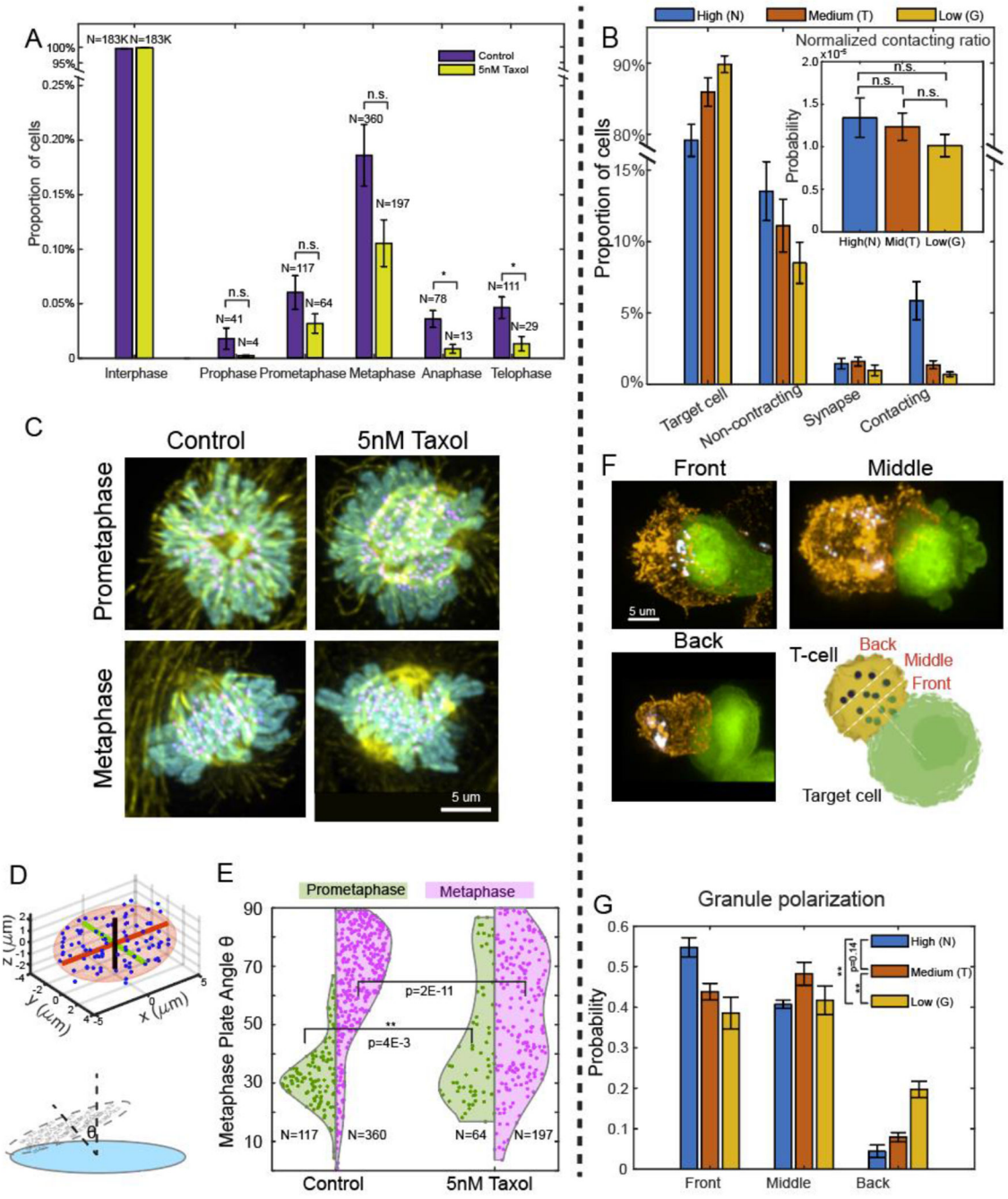

Figure 3: High throughput imaging of Taxol induced mitotic defects and the effect of antigen strength on immune synapses.

(A) Proportion of cells in different mitotic stages for control (purple) and 5 nM Taxol treated (yellow) RPE cells. The number above each bar indicates the total number of cells in the corresponding stage. The data is integrated over three independent samples for each condition, the bar plot and the error bars indicate the mean and the standard error of the mean respectively. *:p<0.05 **(B)** Average proportion of target cells and CTLs with different levels of proximity to target cells (non-contacting, contacting, and synapse). Color

code indicates target cells with different antigen strength (blue: high (N), red: medium (T), yellow: low (G)). Inset: normalized proportion of T cells that are in contact with target cell under high affinity (N), medium affinity (T) and low affinity (G) condition calculated as $\frac{\#\ of\ CTL-synapse+\#\ of\ CTL-contacting}{\#\ of\ total\ CTL*\#\ of\ target\ cell}$. Horizontal bars in the inset show the results of Student's T-test between different target cells antigen strength. Data is integrated over four independent samples for each condition, and the error bar shows the standard error of the mean. **(C)** Representative maximum intensity projections (MIPs) of prometaphase and metaphase cells under control and 5 nM Taxol treated conditions showing chromosomes (cyan), kinetochores (magenta), and microtubules (yellow). **(D)** Diagram for the characterization of kinetochore distributions. Top: anisotropy is defined by the ratio between the variation of the axis with the largest and the smallest variation and is used to determine the metaphase plate orientation (see Methods for details). Bottom: Diagram depicting the metaphase plate orientation relative to z-axis of the microscope objective (see Methods for details). **(E)** Violin plot of metaphase plate angle (θ) for control and 5 nM Taxol treated cells in prometaphase (green) and metaphase (magenta). The colored areas indicate the distribution. Horizontal bars indicate the significance based on the Kolmogorov-Smirnov test (K-S test) between Taxol and control in prometaphase (n = 117 for control and n = 64 for Taxol) and metaphase (n = 360 for control and n = 197 for Taxol). **(F)** Representative MIPs and cartoon of CTL synapses with lytic granules concentrated at front, middle and back of CTLs (See Method for details). **(G)** Histogram of the three types of synapses under different affinity conditions. Blue: high affinity; Red: medium affinity; Yellow: low affinity (n = 317 for high affinity, n = 497 for medium affinity, and n = 334 for low affinity). Data is integrated over four independent samples for each condition. Vertical bars near the legend indicate the significance based on the Kolmogorov–Smirnov test (K-S test) between different target cell antigen strength. **: $p < 0.01$

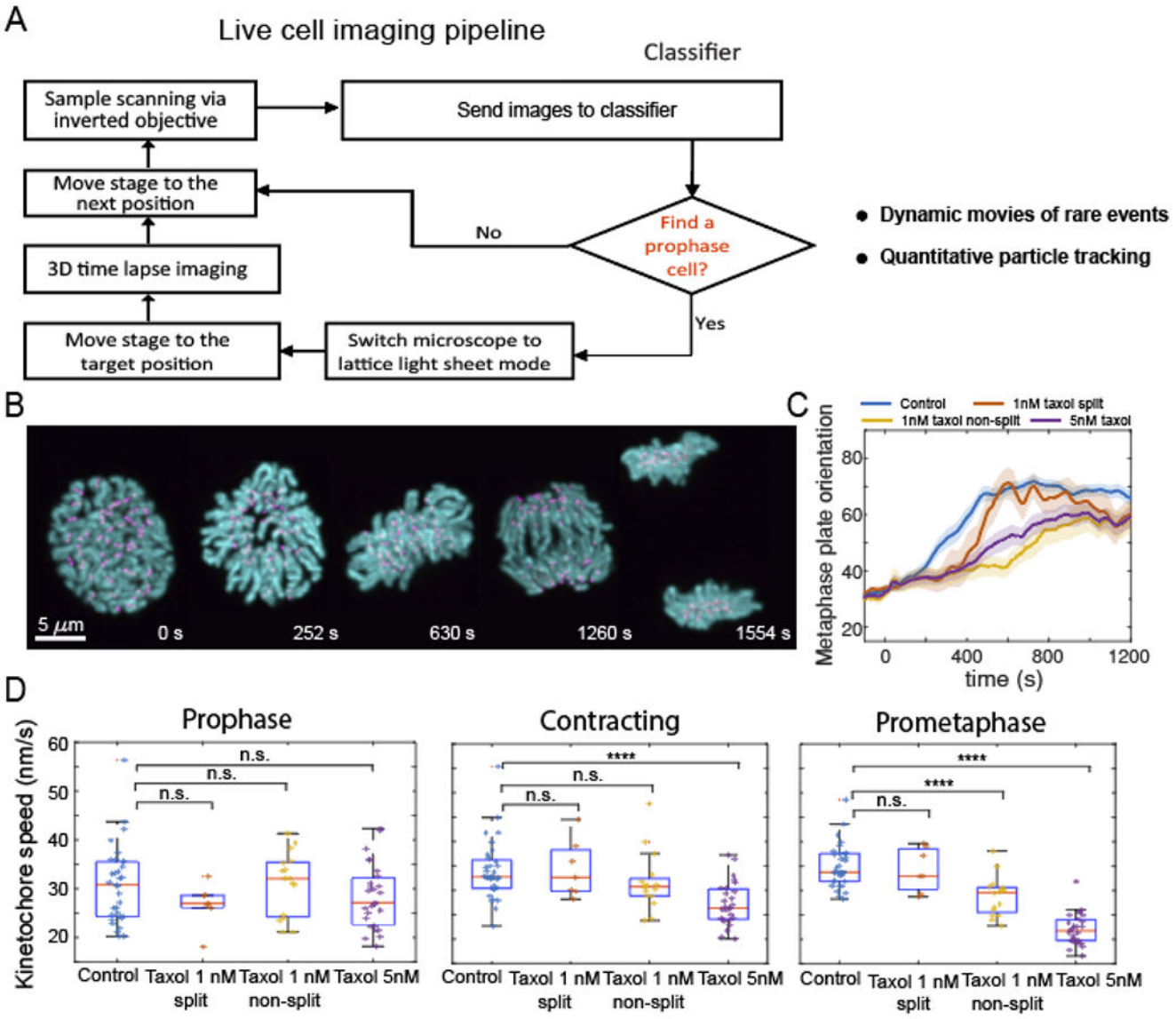

Figure 4: High throughput imaging of kinetochore dynamics during mitosis.

(A) Flow chart for imaging live-sample dynamics. Once a cell in prophase is found, the microscope switches to LLSM imaging to capture a 4D movie of the mitotic process. **(B)** Images show representative time points from a live-cell movie of kinetochores (magenta) and chromosomes (cyan). **(C)** Metaphase plate orientation (θ) plotted over time for each cell. The solid line indicates the average angle at a given time after the start of prometaphase (t = 0 s, see Methods for details) and the shades indicate the standard error across cells. **(D)** Box and whisker plots for the median kinetochore speed of a given cell at a given stage. The box indicates the 25th to 75th percentiles and the horizontal marker indicates the population median. The whiskers extend to the most extreme data that are not considered outliers. All perturbed conditions are compared to the control condition via t-test. n.s.: not significant, ****:p<1E-4. For (C) and (D): control (n = 35), 1 nM Taxol 1 nM split (n = 7), Taxol 1 nM non-split (n=16), and Taxol 5 nM (n = 27)

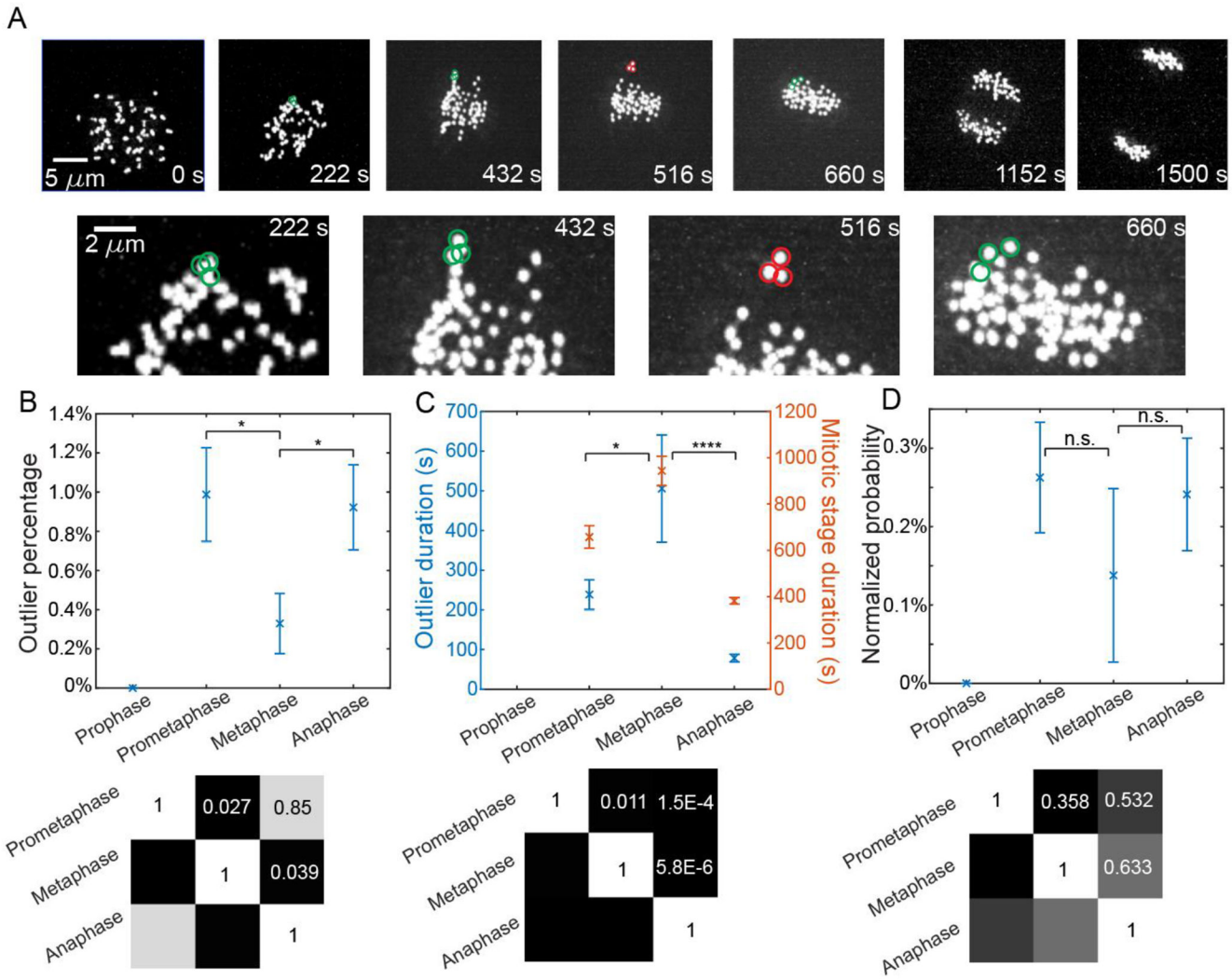

Figure 5: Longitudinal tracking of kinetochore motion during mitosis.

(A) Sample snapshots of the kinetochore trajectories during mitosis. T = 0 s is the start of the movie in prophase. Red circles indicate kinetochores that are identified as outliers. Green circles indicate the locations of outlier kinetochores prior to and after being identified as outliers. **(B)** Plot of the percentage of kinetochores that are considered an outlier in different mitotic stages measured across n = 33 control cell movies. Crosses and error bars indicate the median and the standard error measured across individual cell movies. **(C)** Plot of the durations of outlier events (blue, left axis) and the durations of different mitotic stages (orange, right axis). The crosses and error bars indicate the mean and the standard error of outlier kinetochores detected in different stages: prophase n = 0, prometaphase n = 30, metaphase n = 10, anaphase n = 28. Here n is the number of outlier kinetochores across all 33 control cell movies. **(D)** Plot of the instantaneous probabilities for finding an outlier kinetochore at a given time point in different mitotic stages (see Methods for details). The matrices below B-D show the p-value of the pairwise K-S significant test between prometaphase, metaphase, and anaphase.